Aharonov-Bohm effect in three-dimensional higher-order topological insulators

Kun Luo,[1] Hao Geng,[1,2] Li Sheng,[1,2] Wei Chen ⓞ,[1,2,*] and D. Y. Xing[1,2]

[1]*National Laboratory of Solid State Microstructures and School of Physics, Nanjing University, Nanjing 210093, China*
[2]*Collaborative Innovation Center of Advanced Microstructures, Nanjing University, Nanjing 210093, China*

One-dimensional hinge states are the hallmark of three-dimensional (3D) higher-order topological insulators (HOTIs), which may lead to interesting transport properties. Here, we study the Aharonov-Bohm (AB) effect in an interferometer constructed by the hinge states in normal metal-HOTI junctions with a transverse magnetic field. We show that the AB oscillation of the conductance can clearly manifest the spatial configurations of such hinge states. The magnetic fluxes encircled by various interfering loops are composed of two basic ones, so that the oscillation of the conductance by varying the magnetic field contains different frequency components universally related to each other. Specifically, the four dominant frequencies $\omega_{x,y}$ and $\omega_{x\pm y}$ satisfy the relations $\omega_{x\pm y} = \omega_x \pm \omega_y$, which generally hold for different magnetic fields, sample sizes, bias voltages, and weak disorders. Our results provide a unique and robust signature of the hinge states and pave the way for exploring the AB effect in 3D HOTIs.

I. INTRODUCTION

Over the past two decades, topological phases of matter such as topological insulators and superconductors have become an active research field of condensed matter physics [1,2]. These materials are characterized by nontrivial band topology and the resultant gapless $(d-1)$-dimensional edge states. Very recently, the concepts of higher-order topological insulators (HOTIs) and superconductors were theoretically proposed, which are featured by the $(d-2)$-dimensional edge states [3–17]. Specifically, for three-dimensional (3D) HOTIs there exist one-dimensional (1D) gapless states along the hinges of the sample, so-called hinge states, while the surface and the bulk states are both insulating. Recent progress has shown evidence of hinge states in bismuth by scanning tunneling spectroscopy and Josephson interferometry [17], which paves the way for exploring more intriguing properties of such topological states in HOTIs.

The 1D nature of the hinge states indicates that it is a good playground for exploring various interference effects, such as the Aharonov-Bohm (AB) and Fabry-Pérot interferometers [18–23]. Actually, the chiral edge states of the quantum Hall phase have become an important platform for the study of mesoscopic physics, in which a variety of novel phenomena have been observed [20,24–26] due to its long coherence length and high adjustability. Compared with the chiral edge states, the hinge states in HOTIs open additional possibilities for the implementation of novel effects due to their 3D configurations, which enrich the way of interfering in real space. Moreover, such effects cannot be realized in any two-dimensional (2D) systems, which, in turn, can serve as deterministic evidence of hinge states.

The manifestation of the AB effect in an electron system is the periodic oscillation of conductance as a closed trajec-

tory of electrons encircles a magnetic flux Φ [27–32]. The dominant period of oscillation is equal to the flux quantum $\Phi_0 = h/e$, with a main frequency $2\pi/\Phi_0$. The frequency of oscillation can be found by taking the fast Fourier transform (FFT) of the conductance pattern [28–30]. Recently, the AB effect has been used as an effective way to detect edge states in various topological systems, such as the edge states of topological insulators [33–36], Majorana fermions of topological superconductors [37–40], surface states of topological semimetals [41,42], and non-Abelian anyons of fractional quantum Hall systems [23,43–46].

In this paper, we investigate the AB effect in an interferometer composed of the hinge states of a quadrangular HOTI by imposing an external magnetic field. The insulating bulk and surface states indicate that an electron can only propagate along the hinges of the sample, by which the enclosed magnetic flux can lead to a coherent oscillation of the transmission probability. Different from the edge states in any 2D systems, a 3D network of hinge states results in peculiar interfering trajectories, which rely not only on the magnitude of the magnetic field but also on its orientation. The AB interferometer is sketched in Fig. 1(a), where the HOTI is connected to two leads made of a normal metal and a magnetic field $\boldsymbol{B} = (B_x, B_y) = B(\cos\theta, \sin\theta)$ is applied in the x-y plane, with θ being the polar angle. The electrons injected from the leads propagate along four chiral hinge states, which comprise a variety of interfering loops; see Figs. 1(b)–1(e). The elemental interfering loops shown in Figs. 1(b) and 1(c) are exactly the boundaries of the $(\pm 1, 0, 0)$ and $(0, \pm 1, 0)$ surfaces. The basic loops in Figs. 1(b) and 1(c) encircle a magnetic flux of $\Phi_x = B\cos\theta S_x$ and $\Phi_y = B\sin\theta S_y$, respectively, with $S_{x,y}$ the surface areas. Accordingly, the frequency components $\omega_x = 2\pi\cos\theta S_x/\Phi_0$ and $\omega_y = 2\pi\sin\theta S_y/\Phi_0$ naturally appear in the oscillating pattern of the conductance as the magnetic field B is varied. Interestingly, the magnetic flux in other interfering loops can all be interpreted by the two elemental ones,

*Corresponding author: pchenweis@gmail.com

085427-1
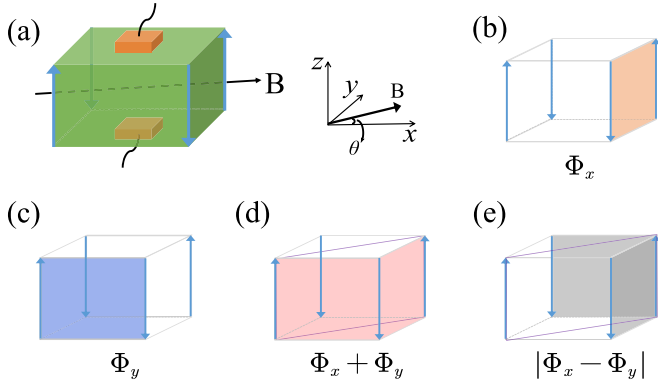
FIG. 1. (a) The interferometer constructed by a HOTI (green block) and normal metal electrodes (orange blocks). The magnetic field B is imposed in the x-y plane with a polar angle θ. (b), (c) Two elemental interfering loops with an encircled flux Φ_x, Φ_y. (d), (e) The other two dominant interfering loops with fluxes $\Phi_x + \Phi_y$, $|\Phi_x - \Phi_y|$.

among which two typical loops in Figs. 1(d) and 1(e) contain a flux of $\Phi_{x\pm y} = \Phi_x \pm \Phi_y$, and the corresponding oscillating frequency components satisfy $\omega_{x\pm y} = \omega_x \pm \omega_y$. It turns out that the aforementioned four interfering loops and the corresponding oscillating frequencies dominate the coherent oscillation of the conductance. The relations $\omega_{x\pm y} = \omega_x \pm \omega_y$ generally hold independent of various parameters such as the magnetic field, sample size, bias voltage, and weak disorder, thus providing a universal and deterministic signature of the hinge states and HOTIs.

The rest of this paper is organized as follows. In Sec. II, we elucidate the model of the HOTI adopted in our work. In Sec. III, we apply the scattering matrix approach to analyze the coherent transport through the interferometer and the AB oscillation of the conductance. Detailed numerical simulations on the lattice model are conducted in Sec. IV, which verify the universality of the physical results. Finally, a brief summary and outlook are given in Sec. V.

II. MODEL OF HOTI

We adopt the model of 3D chiral HOTIs introduced by Schindler *et al.* [7] as

$$H_{\text{HOTI}} = \left(M + t\sum_i \cos k_i\right)\tau_z\sigma_0 + \Delta_1 \sum_i \sin k_i \tau_x\sigma_i \quad (1)$$
$$+ \Delta_2(\cos k_x - \cos k_y)\tau_y\sigma_0,$$

where $\sigma_{i=x,y,z}$ and τ_i are the Pauli matrices acting on the spin and orbital space, respectively. For $1 < |M/t| < 3$ and $\Delta_1, \Delta_2 \neq 0$, the system lies in a chiral 3D HOTI phase. The energy spectra are gapped in both the bulk and four surfaces parallel to the z axis. Importantly, the mass term is opposite in sign between adjacent surfaces that results in the Jackiw-Rebbi-type bound states [47] propagating only along the $\pm z$ direction, or the so-called topological hinge states. Time-reversal symmetry is broken in Eq. (1), so that the hinge states are unidirectional or chiral, without any backscattering states within a given hinge. Notably, gapless Dirac cones pro-

tected by $\hat{C}_4^z\hat{T}$ symmetry persist on the surfaces perpendicular to the z axis [7]. Therefore, it is beneficial to explore the pure signature of the hinge states through transport in the z direction.

III. SCATTERING MATRIX ANALYSIS

In this section, we study the coherent transport of electrons through the interferometer sketched in Fig. 1(a) based on the low-energy effective model of the hinge states using the scattering matrix approach. The scattering matrix of the whole interferometer can be obtained by combining those at two normal metal-HOTI interfaces and the matrix of phase accumulation during propagation in the hinge states. The matrix at the lower interface [cf. Fig. 1(a)] can be parametrized as

$$S_l = \begin{pmatrix} r_1 & r_3 & t_1' & t_3' \\ r_2 & r_4 & t_2' & t_4' \\ t_1 & t_3 & r_1' & r_3' \\ t_2 & t_4 & r_2' & r_4' \end{pmatrix}, \quad (2)$$

which relates the incoming (a_l) and outgoing (b_l) waves in the normal metal and the HOTI via $b_l = S_l a_l$. The matrix is assumed to be 4×4 such that two incoming/outgoing waves are taken into account on both sides. For the HOTI, the number of channels corresponds to that of pairs of hinge states. The unitary condition $S_l S_l^\dagger = I$ is ensured by the law of current conservation. Here, $t_{1,...,4}$ are the transmission amplitudes from the normal metal to the chiral hinge states of the HOTI and $r_{1,...,4}$ are the corresponding reflection amplitudes. The scattering amplitudes corresponding to the incident waves from the hinge states of the HOTI are defined by $t'_{1,...,4}, r'_{1,...,4}$ in a similar way. The scattering matrix for the upper interface can be defined as

$$S_u = \begin{pmatrix} r_1^u & r_3^u & t_1^{u\prime} & t_3^{u\prime} \\ r_2^u & r_4^u & t_2^{u\prime} & t_4^{u\prime} \\ t_1^u & t_3^u & r_1^{u\prime} & r_3^{u\prime} \\ t_2^u & t_4^u & r_2^{u\prime} & r_4^{u\prime} \end{pmatrix}. \quad (3)$$

The phase modulation of the wave function due to the magnetic field can be described by the matrix as

$$S_m = \begin{pmatrix} 0 & 0 & e^{i\tilde{\phi}_1} & 0 \\ 0 & 0 & 0 & e^{-i\tilde{\phi}_2} \\ e^{-i\phi_2} & 0 & 0 & 0 \\ 0 & e^{i\phi_1} & 0 & 0 \end{pmatrix}, \quad (4)$$

where the phases $\phi_1, \phi_2, \tilde{\phi}_1, \tilde{\phi}_2$ are related by the magnetic fluxes through $\phi_1 + \tilde{\phi}_1 = \phi_2 + \tilde{\phi}_2 = \phi_x = 2\pi\Phi_x/\Phi_0$, $\phi_1 - \tilde{\phi}_2 = \phi_2 - \tilde{\phi}_1 = \phi_y = 2\pi\Phi_y/\Phi_0$, $\phi_1 + \phi_2 = \phi_{x+y} = 2\pi\Phi_{x+y}/\Phi_0$, and $\tilde{\phi}_1 + \tilde{\phi}_2 = \phi_{x-y} = 2\pi\Phi_{x-y}/\Phi_0$, with $\phi_{x,y}$ and $\phi_{x\pm y}$ being gauge invariant.

By combining three matrices S_l, S_m, S_u in a standard way we obtain the total scattering matrix for the whole system. Here, we focus on the periods of the AB oscillation and an overall phase shift of the pattern is unimportant. Therefore, we can choose S_l, S_u to be real for simplicity, which will not change the main results. For an electron incident from the
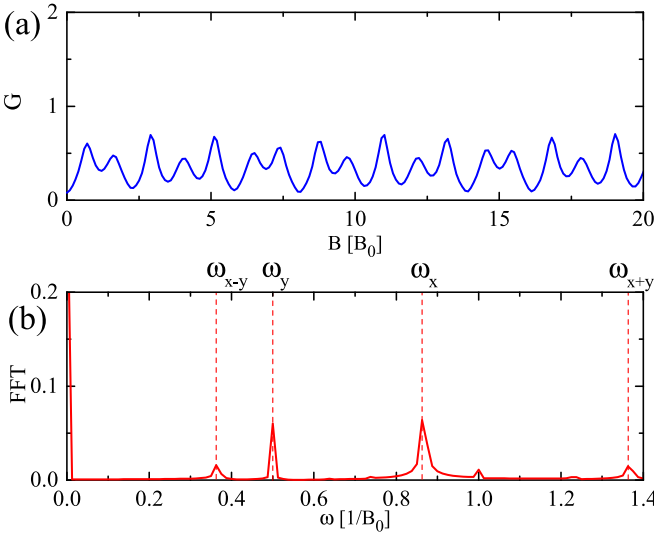
FIG. 2. (a) The conductance pattern calculated by the scattering matrices. (b) The FFT spectrum of the oscillation pattern. The relevant scattering coefficients are set to $t_1 = t_3 = t_4 = r_1' = r_1^u = r_2' = \sqrt{0.4}$, $t_2 = r_3' = \sqrt{0.3}$, $r_1 = r_2' = \sqrt{0.2}$, $r_2 = r_3 = r_4 = t_1^u = t_2^u = t_3^u = \sqrt{0.1}$, $r_4' = t_4^u = -\sqrt{0.1}$, $r_3^u = r_4^u = -\sqrt{0.4}$.

lower terminal, its transmission probability T to the upper terminal is obtained after some algebra as

$$T = F^{-1}[C + C_X \cos \phi_x + C_Y \cos \phi_y + C_{XY} \cos \phi_{x+y}$$
$$+ C_{XY}' \cos \phi_{x-y}],$$
$$F = M_C + M_{XY} \cos \phi_{x+y} + M_{XY}' \cos \phi_{x-y} + M_{2X} \cos(2\phi_x)$$
$$+ M_{2Y} \cos(2\phi_y) - M_X \cos \phi_x - M_Y \cos \phi_y, \quad (5)$$

where the explicit forms of the relevant parameters are given in the Appendix. The numerator of the transmission in Eq. (5) shows that there are four dominant periodic terms contributed by four interference loops in Figs. 1(b)–1(e) which correspond to four frequencies related by $\omega_{x,y}$, $\omega_{x+y} = \omega_x \pm \omega_y$. Note that such relations are stabilized by the spatial configurations of the hinge states, thus offering a clear and robust signature for their detection, which relies little on the sample details and the energy. Although a magnetic field in different directions will change the values of frequencies it does not affect the general relations between them.

Next, we provide numerical verification of such an observation using specific scattering amplitudes. The AB oscillation of the conductance as a function of B and its FFT spectrum are shown in Figs. 2(a) and 2(b), respectively. The polar angle of the magnetic field is set to $\theta = \pi/6$ and the unit of frequency is chosen as $1/B_0$ with $B_0 = \Phi_0/(2\pi S)$ and $S = S_x = S_y$ the surface area. One can find multiple periods in the conductance spectrum in Fig. 2(a). The FFT spectrum in Fig. 2(b) shows that there are four dominant frequencies with $\omega_x = 0.86/B_0$, $\omega_y = 0.5/B_0$, $\omega_{x-y} = 0.36/B_0$, $\omega_{x+y} = 1.36/B_0$, which conforms the aforementioned relations $\omega_{x\pm y} = \omega_x \pm \omega_y$. Higher frequencies such as ω_{2x}, ω_{2y} should also appear as that in the conventional 2D AB effect. In stark contrast, the frequencies $\omega_{x\pm y}$ can only exist in a 3D HOTI, which thus provides unique evidence of the hinge states.

IV. LATTICE MODEL SIMULATION

Based on the scattering matrix analysis, we see that there are four dominant frequencies satisfying the universal relations $\omega_{x\pm y} = \omega_x \pm \omega_y$. In this section, we perform numerical simulation to give rigorous results. We write the model in Eq. (1) on a cubic lattice as [48]

$$H_{\text{HOTI}}^{\text{Lattice}} = \sum_i c_i^\dagger M \sigma_0 \tau_z c_i$$
$$+ \left\{ \sum_i c_{i+x}^\dagger \left[\frac{e^{i\varphi_x}}{2} (\Delta_2 \sigma_0 \tau_y + t\sigma_0 \tau_z + i\Delta_1 \sigma_x \tau_x) \right] c_i \right.$$
$$- \sum_i c_{i+y}^\dagger (\Delta_2 \sigma_0 \tau_y + t\sigma_0 \tau_z + i\Delta_1 \sigma_y \tau_x) c_i$$
$$\left. + \sum_i c_{i+z}^\dagger \frac{e^{i\varphi_z}}{2} (t\sigma_0 \tau_z + i\Delta_1 \sigma_z \tau_x) c_i + \text{H.c.} \right\}, \quad (6)$$

where $c_i = (c_{a,\uparrow,i}, c_{b,\uparrow,i}, c_{a,\downarrow,i}, c_{b,\downarrow,i})$ are the annihilation operators at lattice site i with two spin $(\uparrow, \downarrow)$ and two orbit (a, b) components. The Peierls phase $\varphi_{x,z} = \frac{e}{\hbar} \int_{r_i}^{r_j} A(r) \cdot dr$, where $A(r) = (B_y z, 0, B_x y)$ is the vector potential under the Landau gauge. The lattice model of the normal metal electrodes is

$$H_{\text{NM}} = \sum_i (-6t + U) c_i^\dagger c_i + \sum_i t(c_{i+x}^\dagger c_i$$
$$+ c_{i+y}^\dagger c_i + c_{i+z}^\dagger c_i) + \text{H.c.} \quad (7)$$

An AB interferometer constructed of a 3D HOTI (green block) and normal metal leads (two orange blocks) is shown in Fig. 1(a). The blue arrowed lines denote the chiral hinge states. The cross section of the HOTI in the x-y plane is set as $30a \times 30a$ and that for the normal metal leads is $5a \times 5a$ with a being the lattice constant. The magnetic field B exists only in the HOTI region and is parallel to the x-y plane.

Consider an electron impinging from the normal metal towards the HOTI with its energy lying in the bulk gap ($\simeq 0.7|t|$) and surface gap ($\simeq 0.32|t|$) of the HOTI, so that only the hinge channels are available for propagation. Backscattering can occur at the interfaces, giving rise to various interference loops. The two-terminal conductance G is calculated using the KWANT package [49] and the AB conductance oscillation for different incident energies (ie) and polar angles θ of the magnetic field are shown in Fig. 3(a) (curves are offset by $2e^2/h$ for clarity). To get the dominant frequencies, we perform FFT calculations whose spectra are shown in Figs. 3(b) and 3(c).

The numerical results are consistent with those by the scattering matrix analysis in Fig. 2(b). For different incident energies, the oscillation patterns in Fig. 3(a) appear to be starkly different. However, the dominant frequencies remain almost the same; see Fig. 3(b). To check the general relations between oscillation frequencies, we first locate two notable peaks ω_x and ω_y by the dashed lines and the other two peaks $\omega_{x\pm y} = \omega_x \pm \omega_y$ are marked accordingly in Fig. 3(b). One can see that the dominant peaks match the dashed lines very well apart from a small deviation from ω_{x+y} for $ie = 0.1$, which is attributed to the limit of the numerical calculations. For different polar angles θ, similar results can be seen in Fig. 3(c).
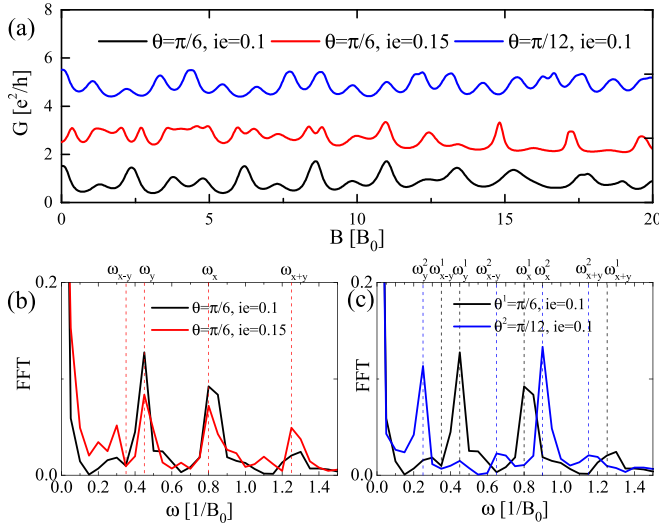
FIG. 3. (a) Conductance oscillation for different incident energies and angles θ by the lattice simulation. An offset $2e^2/h$ is imposed to adjacent curves for clarity. (b), (c) Corresponding FFT spectra of the conductance patterns. Four dominant frequencies are marked by the dashed lines. The model parameters are set to $t = -1$, $M = 2.3$, $\Delta_1 = 0.8$, $\Delta_2 = 0.5$, $U = 2$. The lattice of the HOTI is set to a $30a \times 30a \times 30a$ cube, where $a = 1$ is the lattice constant.

Although the locations of the peaks change for different θ, the general relations between them persist.

In Fig. 4, we present more general results by varying both the polar angle θ and the thickness of the HOTI in the z direction. Each pair of parameters generates one point in both Figs. 4(a) and 4(b), with its coordinates extracted in the same way as done in Fig. 3(b). The reference planes therein correspond to the frequency rule $\omega_{x\pm y} = \omega_x \pm \omega_y$. One can see that the numerical results labeled by the black and orange dots are well located around the reference planes, which indicates the universality of the frequency rules. Note that there are a few dots of negative frequencies in Fig. 4(b) for $\omega_x < \omega_y$. In experiments, one should rather measure $|\omega_x - \omega_y|$ instead.

Disorder generally exists in real samples and it can be expected that topological chiral hinge states and thus the AB effect should be robust, the same as that in the quantum Hall edge states. We show numerical results for the disorder distributed in the whole HOTI region in Fig. 5 with different strengths α. For a weak disorder strength $\alpha < 0.7|t|$ (the gap of the bulk states), the oscillation pattern and frequency rules $\omega_{x\pm y} = \omega_x \pm \omega_y$ are retained. For a strong disorder $\alpha > 0.7|t|$, the oscillation pattern quenches stem from disorder-induced coupling between the surface/bulk states and the hinge states. Therefore, as long as the disorder in the sample of HOTI is not too strong, the AB effect can be hopefully observed. A similar conclusion also holds for the surface roughness. Although the AB effect is quite robust against the disorder effect, the observation should be carried out within the phase coherence length of the system. The dephasing effect always reduces the visibility of the coherent oscillation until it vanishes [30,50]. One more remark is that the interference here is all of the AB type without an Al'tshuler-Aronov-Spivak (AAS)-type con-
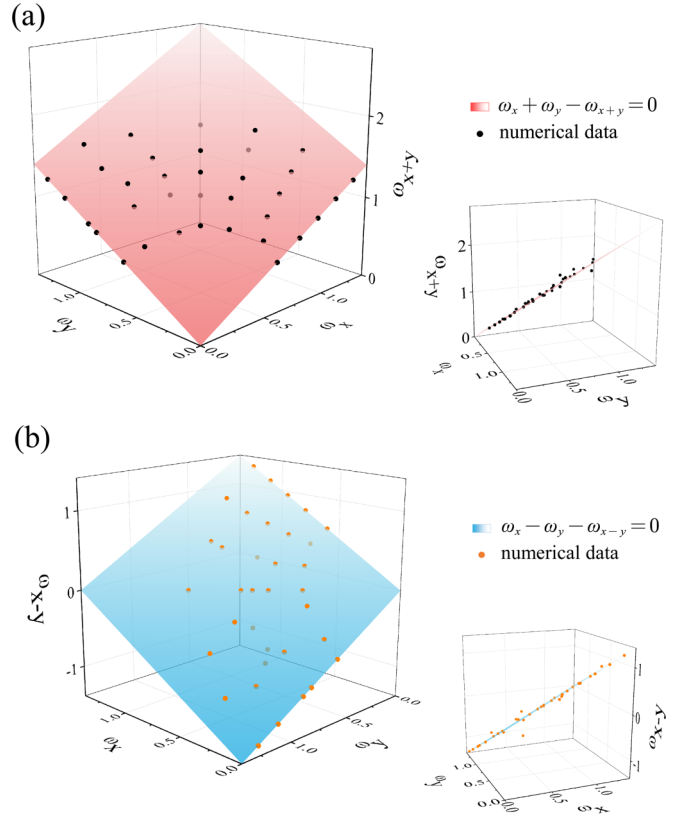
FIG. 4. (a) ω_{x+y} and (b) ω_{x-y} as a function of elemental frequencies ω_x and ω_y. Black and orange dots denote numerical results for different lengths of the HOTI and polar angles θ of the magnetic field. The reference planes satisfy $\omega_{x\pm y} = \omega_x \pm \omega_y$. Insets: Side view of the plots which reveal the deviation of the dots from the planes. The parameters are the same as those in Fig. 3.

tribution [51–53]. The model in Eq. (1) breaks time-reversal symmetry so that the AAS effect is absent.
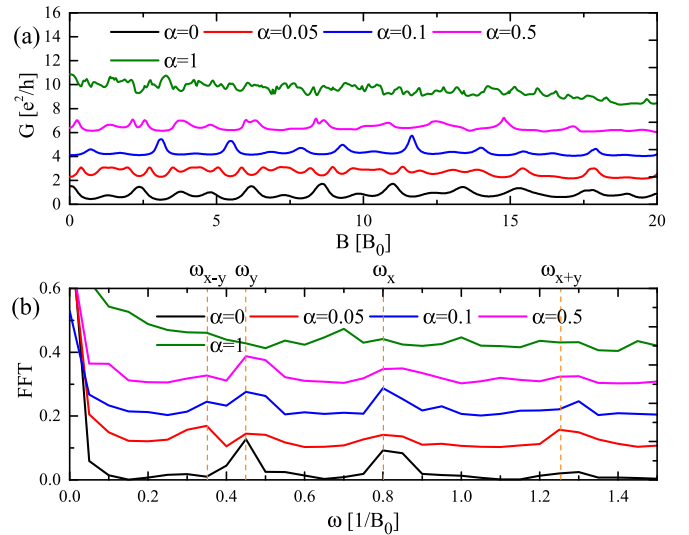
FIG. 5. (a) Conductance patterns with different disorder strengths α. (b) FFT spectra of the conductance. The incident energy is $ie = 0.1$ and the polar angle of the field is $\theta = \pi/6$. Other parameters are the same as those in Fig. 3.

V. SUMMARY AND OUTLOOK

In summary, we have investigated the AB effect in the chiral hinge states of a 3D HOTI. Due to the spatial configurations of the hinge states, different types of interfering loops appear compared with 2D AB interference. Importantly, we predict a universal relations $\omega_{x\pm y} = \omega_x \pm \omega_y$ between the dominant oscillating frequencies, which offers a unique signature of the hinge states as well as the HOTI. Our study can be generalized straightforwardly to the AB effect in 3D HOTIs with helical hinge states.

Note added. Recently, we became aware of a related work [54], which focuses on different aspects.

APPENDIX: SPECIFIC FORMS OF COEFFICIENT FOR ANALYSIS CALCULATION

In Eq. (5) of the main text, the coefficients are expressed as

$$
\begin{aligned}
C &= \left(t_1^2 + t_3^2\right)\left(W_0^2 + W_1^2 + W_2^2 + X_0^2 + X_1^2 + X_2^2\right) + \left(t_2^2 + t_4^2\right)\left(Y_0^2 + Y_1^2 + Y_2^2 + Z_0^2 + Z_1^2 + Z_2^2\right), \\
C_X &= 2(W_0 W_1 + X_0 X_1)\left(t_1^2 + t_3^2\right) + 2(Y_0 Y_1 + Z_0 Z_1)\left(t_2^2 + t_4^2\right) + 2(W_0 Y_2 + W_2 Y_0 + X_0 Z_2 + X_2 Z_0)(t_1 t_2 + t_3 t_4), \\
C_Y &= 2(W_0 W_2 + X_0 X_2)\left(t_1^2 + t_3^2\right) + 2(Y_0 Y_2 + Z_0 Z_2)\left(t_2^2 + t_4^2\right) + 2(W_0 Y_1 + W_1 Y_0 + X_0 Z_1 + X_1 Z_0)(t_1 t_2 + t_3 t_4), \\
C_{XY} &= 2(W_0 Y_0 + W_0 Y_0)(t_1 t_2 + t_3 t_4), \\
C'_{XY} &= 2(W_1 W_2 + X_1 X_2)\left(t_1^2 + t_3^2\right) + 2(Y 1 Y_2 + Z_1 Z_2)\left(t_2^2 + t_4^2\right) + 2(W_1 Y_1 + W_2 Y_2 + X_1 Z_1 + X_2 Z_2)(t_1 t_2 + t_3 t_4), \\
M_{XY} &= 2M_1 M_4 + 2M_2 M_3, \quad M'_{XY} = 2M_1 M_3 + 2M_2 M_4, \quad M_{2X} = 2M_1 M_2, \quad M_{2Y} = 2M_3 M_4, \\
M_X &= 2M_0 M_1 + 2M_0 M_2, \quad M_Y = 2M_0 M_3 + 2M_0 M_4, \quad M_C = M_0^2 + M_1^2 + M_2^2 + M_3^2 + M_4^2,
\end{aligned}
\tag{A1}
$$

which contain the parameters defined by the elements of the scattering matrices as

$$
\begin{aligned}
W_0 &= t_1^u, & W_1 &= t_3^u r_2' r_1^u - t_1^u r_2' r_3^u, & W_2 &= t_3^u r_4' r_2^u - t_1^u r_4' r_4^u, \\
X_0 &= t_2^u, & X_1 &= t_4^u r_2' r_1^u - t_2^u r_2' r_3^u, & X_2 &= t_4^u r_4' r_2^u - t_2^u r_4' r_4^u, \\
Y_0 &= t_3^u, & Y_1 &= t_1^u r_3' r_4^u - t_3^u r_3' r_2^u, & Y_2 &= t_1^u r_1' r_3^u - t_3^u r_1' r_1^u, \\
Z_0 &= t_4^u, & Z_1 &= t_2^u r_3' r_4^u - t_4^u r_3' r_2^u, & Z_2 &= t_2^u r_1' r_3^u - t_4^u r_1' r_1^u, \\
M_0 &= 1 + r_1' r_1^u r_4' r_4^u + r_3' r_2^u r_2' r_3^u - r_1' r_3^u r_4' r_2^u - r_3' r_4^u r_2' r_1^u, \\
M_1 &= r_2' r_3^u, & M_2 &= r_3' r_2^u, & M_3 &= r_4' r_4^u, & M_4 &= r_1' r_1^u.
\end{aligned}
\tag{A2}
$$

[1] X.-L. Qi and S.-C. Zhang, Rev. Mod. Phys. **83**, 1057 (2011).

[2] M. Z. Hasan and C. L. Kane, Rev. Mod. Phys. **82**, 3045 (2010).

[3] W. A. Benalcazar, B. A. Bernevig, and T. L. Hughes, Science **357**, 61 (2017).

[4] W. A. Benalcazar, B. A. Bernevig, and T. L. Hughes, Phys. Rev. B **96**, 245115 (2017).

[5] Z. Song, Z. Fang, and C. Fang, Phys. Rev. Lett. **119**, 246402 (2017).

[6] J. Langbehn, Y. Peng, L. Trifunovic, F. von Oppen, and P. W. Brouwer, Phys. Rev. Lett. **119**, 246401 (2017).

[7] F. Schindler, A. M. Cook, M. G. Vergniory, Z. Wang, S. S. Parkin, B. A. Bernevig, and T. Neupert, Sci. Adv. **4**, eaat0346 (2018).

[8] S. Franca, J. van den Brink, and I. C. Fulga, Phys. Rev. B **98**, 201114(R) (2018).

[9] M. J. Park, Y. Kim, G. Y. Cho, and S. B. Lee, Phys. Rev. Lett. **123**, 216803 (2019).

[10] E. Khalaf, Phys. Rev. B **97**, 205136 (2018).

[11] D. D. Vu, R.-X. Zhang, and S. Das Sarma, Phys. Rev. Research **2**, 043223 (2020).

[12] R.-X. Zhang, Y.-T. Hsu, and S. Das Sarma, Phys. Rev. B **102**, 094503 (2020).

[13] Z. Yan, Phys. Rev. Lett. **123**, 177001 (2019).

[14] D. Călugăru, V. Juričić, and B. Roy, Phys. Rev. B **99**, 041301(R) (2019).

[15] Z. Yan, Phys. Rev. B **100**, 205406 (2019).

[16] Z. Yan, F. Song, and Z. Wang, Phys. Rev. Lett. **121**, 096803 (2018).

[17] F. Schindler, Z. Wang, M. G. Vergniory, A. M. Cook, A. Murani, S. Sengupta, A. Y. Kasumov, R. Deblock, S. Jeon, I. Drozdov *et al.*, Nat. Phys. **14**, 918 (2018).

[18] W. Liang, M. Bockrath, D. Bozovic, J. H. Hafner, M. Tinkham, and H. Park, Nature (London) **411**, 665 (2001).

[19] B. J. van Wees, L. P. Kouwenhoven, C. J. P. M. Harmans, J. G. Williamson, C. E. Timmering, M. E. I. Broekaart, C. T. Foxon, and J. J. Harris, Phys. Rev. Lett. **62**, 2523 (1989).

[20] Y. Ji, Y. Chung, D. Sprinzak, M. Heiblum, D. Mahalu, and H. Shtrikman, Nature (London) **422**, 415 (2003).

[21] N. Ofek, A. Bid, M. Heiblum, A. Stern, V. Umansky, and D. Mahalu, Proc. Natl. Acad. Sci. U.S.A. **107**, 5276 (2010).

[22] D. T. McClure, Y. Zhang, B. Rosenow, E. M. Levenson-Falk, C. M. Marcus, L. N. Pfeiffer, and K. W. West, Phys. Rev. Lett. **103**, 206806 (2009).

[23] J. Nakamura, S. Fallahi, H. Sahasrabudhe, R. Rahman, S. Liang, G. C. Gardner, and M. J. Manfra, Nat. Phys. **15**, 563 (2019).

[24] M. Henny, S. Oberholzer, C. Strunk, T. Heinzel, K. Ensslin, M. Holland, and C. Schönenberger, Science **284**, 296 (1999).

[25] I. Neder, N. Ofek, Y. Chung, M. Heiblum, D. Mahalu, and V. Umansky, Nature (London) **448**, 333 (2007).

[26] E. Weisz, H. Choi, I. Sivan, M. Heiblum, Y. Gefen, D. Mahalu, and V. Umansky, Science **344**, 1363 (2014).

[27] Y. Aharonov and D. Bohm, Phys. Rev. **115**, 485 (1959).

[28] R. A. Webb, S. Washburn, C. P. Umbach, and R. B. Laibowitz, Phys. Rev. Lett. **54**, 2696 (1985).

[29] G. W. Holloway, D. Shiri, C. M. Haapamaki, K. Willick, G. Watson, R. R. LaPierre, and J. Baugh, Phys. Rev. B **91**, 045422 (2015).

[30] A. Lahiri, K. Gharavi, J. Baugh, and B. Muralidharan, Phys. Rev. B **98**, 125417 (2018).

[31] I. L. Aleiner, A. V. Andreev, and V. Vinokur, Phys. Rev. Lett. **114**, 076802 (2015).

[32] Y. Tserkovnyak and B. I. Halperin, Phys. Rev. B **74**, 245327 (2006).

[33] H. Peng, K. Lai, D. Kong, S. Meister, Y. Chen, X.-L. Qi, S.-C. Zhang, Z.-X. Shen, and Y. Cui, Nat. Mater. **9**, 225 (2010).

[34] J. H. Bardarson, P. W. Brouwer, and J. E. Moore, Phys. Rev. Lett. **105**, 156803 (2010).

[35] Y. Zhang and A. Vishwanath, Phys. Rev. Lett. **105**, 206601 (2010).

[36] E. Xypakis, J.-W. Rhim, J. H. Bardarson, and R. Ilan, Phys. Rev. B **101**, 045401 (2020).

[37] J. Li, G. Fleury, and M. Büttiker, Phys. Rev. B **85**, 125440 (2012).

[38] A. Ueda and T. Yokoyama, Phys. Rev. B **90**, 081405(R) (2014).

[39] K. M. Tripathi, S. Das, and S. Rao, Phys. Rev. Lett. **116**, 166401 (2016).

[40] T. C. Bartolo, J. S. Smith, B. Muralidharan, C. Müller, T. M. Stace, and J. H. Cole, Phys. Rev. Research **2**, 043430 (2020).

[41] L.-X. Wang, C.-Z. Li, D.-P. Yu, and Z.-M. Liao, Nat. Commun. **7**, 10769 (2016).

[42] B.-C. Lin, S. Wang, L.-X. Wang, C.-Z. Li, J.-G. Li, D. Yu, and Z.-M. Liao, Phys. Rev. B **95**, 235436 (2017).

[43] E.-A. Kim, Phys. Rev. Lett. **97**, 216404 (2006).

[44] B. I. Halperin, A. Stern, I. Neder, and B. Rosenow, Phys. Rev. B **83**, 155440 (2011).

[45] R. L. Willett, C. Nayak, K. Shtengel, L. N. Pfeiffer, and K. W. West, Phys. Rev. Lett. **111**, 186401 (2013).

[46] J. Nakamura, S. Liang, G. C. Gardner, and M. J. Manfra, Nat. Phys. **16**, 931 (2020).

[47] R. Jackiw and C. Rebbi, Phys. Rev. D **13**, 3398 (1976).

[48] B. A. Levitan and T. Pereg-Barnea, Phys. Rev. Research **2**, 033327 (2020).

[49] C. W. Groth, M. Wimmer, A. R. Akhmerov, and X. Waintal, New J. Phys. **16**, 063065 (2014).

[50] R. Golizadeh-Mojarad and S. Datta, Phys. Rev. B **75**, 081301(R) (2007).

[51] B. L. Al'tshuler, A. G. Aronov, and B. Z. Spivak, JETP Lett. **33**, 94 (1981).

[52] D. Y. Sharvin and Y. V. Sharvin, JETP Lett. **34**, 272 (1981).

[53] B. L. Al'tshuler, A. G. Aronov, B. Z. Spivak, D. Y. Sharvin, and Y. V. Sharvin, JETP Lett. **35**, 588 (1982).

[54] C.-A. Li, S.-B. Zhang, J. Li, and B. Trauzettel, Phys. Rev. Lett. **127**, 026803 (2021).